Magnetotransport properties of the kagome magnet $TmMn_6Sn_6$

Bin Wang,[1] Enkui Yi,[1] Leyi Li,[1] Jianwei Qin,[1] Bing-Feng Hu,[2] Bing Shen,[1,3,*] and Meng Wang[1,†]

[1]*Center for Neutron Science and Technology, Guangdong Provincial Key Laboratory of Magnetoelectric Physics and Devices, School of Physics, Sun Yat-sen University, Guangzhou 510275, China*

[2]*Key Laboratory of Neutron Physics, Institute of Nuclear Physics and Chemistry, China Academy of Engineering Physics, Mianyang 621999, China*

[3]*State Key Laboratory of Optoelectronic Materials and Technologies, Sun Yat-sen University, Guangzhou, Guangdong 510275, China*

(Received 15 May 2022; accepted 24 August 2022; published 7 September 2022)

A kagome magnet usually hosts nontrivial electronic or magnetic states, drawing great interest in condensed matter physics. In this paper, we report a systematic study on the transport properties of the kagome magnet $TmMn_6Sn_6$. The prominent topological Hall effect (THE) has been observed in a wide temperature region spanning over several magnetic phases and exhibiting strong temperature and field dependence. This phenomenon, due to nonzero spin chirality, indicates the possible appearance of nontrivial magnetic states accompanying by strong fluctuations. The planar applied field drives the planar Hall effect and anisotropic magnetoresistivity, exhibiting sharp disconnections in angular-dependent planar resistivity violating the empirical law. By using an effective field, we identify a magnetic transition separating the planar anisotropic magnetoresistivity into two groups belonging to various magnetic states. We extended the empirical formula to scale the field- and temperature-dependent planar magnetoresistivity and provide an understanding of the planar transport behaviors with the crossover between various magnetic states. Our results shed light on the transport effects in the presence of multiple nontrivial magnetic states for a kagome lattice with complicated magnetic structures.

DOI: 10.1103/PhysRevB.106.125107

I. INTRODUCTION

Kagome magnets have emerged as an important platform to study electronic correlations and nontrivial topology [1–6]. The unique crystal structure, made of corner-sharing triangles, naturally has relativistic band crossings at the Brillouin zone corners hosting nontrivial topological electronic Dirac fermions and a dispersionless flat band [7]. With the inclusion of spin-orbital coupling and magnetism, the system can host various nontrivial topological electronic or magnetic states such as magnetic Weyl fermions, quantized anomalous Hall states, nonzero spin texture, etc. [1,8]. Fabricating various magnetic structures in kagome compounds would effectively engineer exotic states with novel phenomena to study the interplay between electrons and magnetism in condensed matter physics.

Recently, a rare-earth family of kagome magnets RMn_6Sn_6 (R stands for rare-earth elements) with a layered hexagonal structure has drawn great interest due to their rich magnetic states and various nontrivial topological band structures [9–16]. These materials usually consist of two submagnetic lattices from different layers: (1) a magnetic kagome lattice consisting of Mn ions, and (2) another magnetic lattice consisting of rare-earth ions. The intra- or interlayer magnetic interactions drive various magnetic structures and complicated magnetic phase diagrams. $TmMn_6Sn_6$ is typical of these materials [16–19]. It forms a hexagonal $P6/mmm$ structure ($a = 5.514$ Å, and $c = 8.994$ Å) consisting of a Mn_3Sn layer (where Mn atoms form the kagome plane) separated by two inequivalent Sn_2 and Sn_2Tm layers as shown in Fig. 1(a). The temperature-dependent resistivity reveals $TmMn_6Sn_6$ is a good metal with small anisotropy. The sharp kinks observed around 325 K in the temperature-dependent magnetization [$M(T)$] curves reveal a magnetic transition shown in Fig. 1(d). Below this transition, the collinear-antiferromagnetic structure transits to a helimagnetic structure which is revealed by neutron scattering measurements and predicted to host chiral spin textures such as skymions [20–22]. Compared with the light rare-earth elements such as Y, Tm is a heavy rare-earth element with $4f$ electrons and strong spin-orbital coupling which may lead to stronger magnetic interactions hosting more complicated magnetic states.

In this paper, we systematically studied the magnetotransport properties of $TmMn_6Sn_6$. Prominent topological Hall effects are observed with an applied field in the ab plane, suggesting the emergence of exotic magnetic states with strong fluctuations. In the presence of magnetic transitions, the planar Hall effect (PHE) and planar anisotropic magnetoresistivity (PAMR) do not obey the empirical law. Especially for PAMR, the abrupt disconnections due to magnetic moment flops separate planar longitudinal resistivity ρ_{xx}^P into different groups belonging to various magnetic states. To describe these transport behaviors, we scaled ρ_{xx}^P by defining an effective field $\mu_0 H^e$ to acquire the critical field. By using a modified empirical law, we described angular-dependent ρ_{xx}^P at various fields and provide the reasoning for these planar transport behaviors spanning over various magnetic states.

*Corresponding author: shenbingdy@mail.sysu.edu.cn
†Corresponding author: wangmeng5@mail.sysu.edu.cn

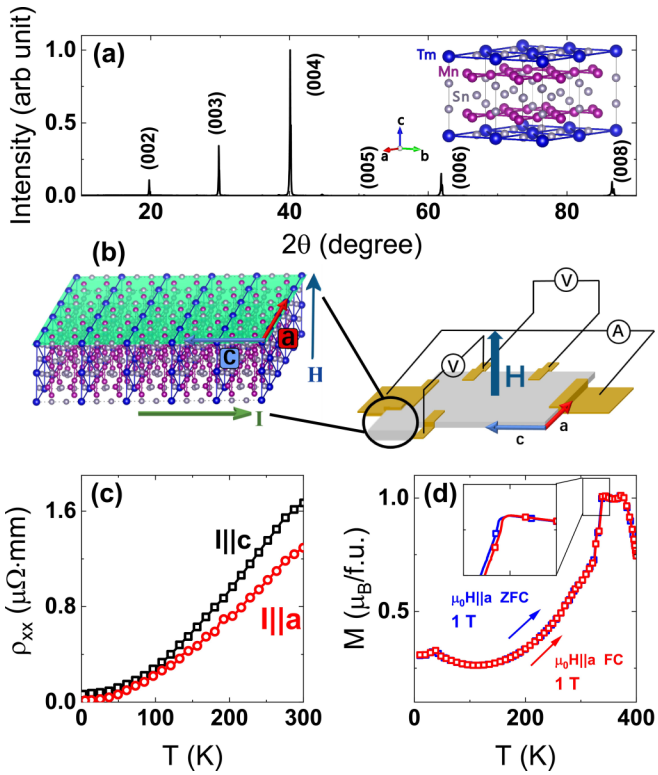

FIG. 1. (a) X-ray diffraction pattern of single-crystalline $TmMn_6Sn_6$ with the corresponding Miller indices $(00l)$ in parentheses. Inset: Crystal structure of $TmMn_6Sn_6$. (b) Schematic for our electronic measurement device of $TmMn_6Sn_6$. (c) Temperature-dependent longitudinal resistivity of $TmMn_6Sn_6$ with the current (I) along the c axis (black line) and a axis (red line). (d) Temperature-dependent magnetization of $TmMn_6Sn_6$ with $\mu_0 H = 1$ T of the $\mu_0 H \parallel a$ zero-field-cooling process (ZFC) (blue line), and $\mu_0 H \parallel a$ field cooling (FC) (marked by the red line), showing they almost overlap. Inset: Partial enlargement of the curve.

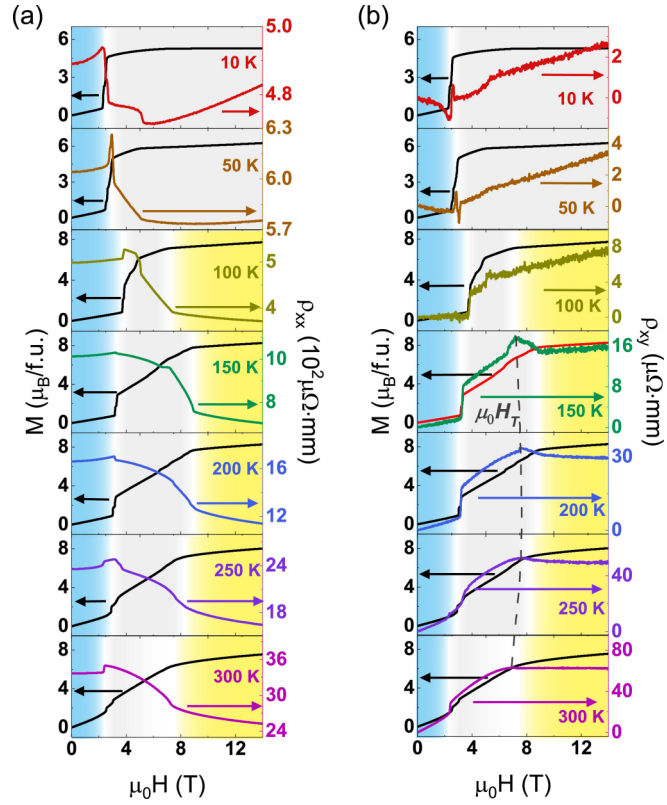

FIG. 2. Field-dependent magnetization $M(\mu_0 H)$, longitudinal resistivity $\rho_{xx}(\mu_0 H)$, and Hall resistivity $\rho_{xy}(\mu_0 H)$ at various temperatures. Based on different slopes of $M(\mu_0 H)$, the curves can be roughly divided into three regions: region 1 marked by the blue shadow, region 2 marked by the light gray shadow, and region 3 marked by the yellow shadow. (a) $M(\mu_0 H)$ (left) and $\rho_{xx}(\mu_0 H)$ (right) at 10, 50, 100, 150, 200, 250, and 300 K with $\mu_0 H \perp ac$. (b) $M(\mu_0 H)$ (left) and $\rho_{xy}(\mu_0 H)$ (right) at the same temperature as shown in (a). Distinct peaks in Hall resistivity $\rho_{xy}(\mu_0 H)$ can be observed at the characteristic field $\mu_0 H_T$.

II. EXPERIMENTAL DETAILS

Single crystals of $TmMn_6Sn_6$ were grown via the self-flux method. Tm, Mn, and Sn metals were mixed and sealed inside an evacuated quartz tube. After that, the mixture was first heated to 1100 °C and then slowly cooled to 550 °C where the flux was removed by using a centrifuge. Large plates of single crystals were obtained with a typical size of $5 \times 5 \times 1$ mm^3. The crystal structure and elemental composition were confirmed by x-ray diffraction (XRD) measurements and energy-dispersive x-ray spectroscopy (EDS). The $[00l]$ peaks were observed in XRD patterns indicating the high quality of our crystals as shown in Fig. 1(a). The selected single crystals were shaped into a rectangular slice for the electric and magnetic transport measurements. Six gold contacts were made on the ac plane with the current along the c axis of crystals as shown in Fig. 1(b). Electrical transport measurements were performed in a physical properties measurement system (PPMS Dynacool, Quantum Design). Magnetization measurements were performed in the vibrating sample magnetometer (VSM) module of the PPMS.

III. RESULTS AND DISCUSSION

A. Topological Hall effect

Field-dependent magnetization $M(\mu_0 H)$, and longitudinal and Hall resistivity [$\rho_{xx}(\mu_0 H)$ and $\rho_{xy}(\mu_0 H)$] are shown in Fig. 2 with the applied field perpendicular to the ac plane ($\mu_0 H \perp ab$). $M(\mu_0 H)$ curves exhibit several obvious kinks and nonmonotonic field dependence, suggesting the emergence of multiple magnetic phase transitions, consistent with previous results [16]. Based on different slopes of $M(\mu_0 H)$, two critical fields $\mu_0 H_{c1}$ and $\mu_0 H_s$ are identified and divide the magnetic phase diagram roughly into three regions (1, 2, and 3). In fact, around $\mu_0 H_{c1}$ multiple transitions are observed. But since these transitions are very close, we denote the metamagnetic transition field by a single variable $\mu_0 H_{c1}$ in this paper. With decreasing the temperature T from 300 to 150 K, $\mu_0 H_{c1}$ and $\mu_0 H_s$ shift to higher fields. Below 100 K with further decreasing T, $\mu_0 H_{c1}$ shifts to lower fields gradually, while $\mu_0 H_s$ moves out of our measurement range rapidly. In region 1 ($\mu_0 H \leqslant \mu_0 H_{c1}$), $\rho_{xx}(\mu_0 H)$ exhibits a positive field response. With increasing $\mu_0 H$, $\rho_{xx}(\mu_0 H)$ exhibits negative magnetoresistivity in regions 2 and 3 with

a slope changing around $\mu_0 H_s$ as shown in Fig. 2(a). Correspondingly, $\rho_{xy}(\mu_0 H)$ exhibits a different field dependence in various regions with the slope changing at the corresponding critical fields. Especially, it is noticed that in region 2, a prominent peak is observed at a characteristic field $\mu_0 H_T$. This anomaly disappears around 100 K with decreasing T. In a magnetic system, the Hall effect generally originates from two contributions: (1) a normal Hall effect (NHE) due to the Lorentz force and (2) an anomalous Hall effect (AHE) due to magnetization or Berry curvature. For $TmMn_6Sn_6$, the discrepancy between ρ_{xy} and M around H_T suggests an additional contribution from the topological Hall effect (THE) besides NHE and AHE. Thus, the total Hall resistivity can be expressed as

$$\rho_{xy} = \rho_{xy}^N + \rho_{xy}^A + \rho_{xy}^T = R_0 \mu_0 H + S_H \rho_{xx}^2 M + \rho_{xy}^T, \quad (1)$$

where R_0 is the Hall coefficient, S_H is a constant for the intrinsic anomalous Hall conductivity ($\sigma_{xy}^A \sim \rho_{xy}^A / \rho_{xx}^2$), which is linearly proportional to M, and ρ_{xy}^N, ρ_{xy}^A, and ρ_{xy}^T are the normal Hall resistivity, anomalous Hall resistivity, and topological Hall resistivity, respectively [23,24]. According to this formula, the curves of $\rho_{xy}(\mu_0 H)/\mu_0 H$ vs $\rho_{xx}(\mu_0 H)^2 M(\mu_0 H)/\mu_0 H$ at various temperatures are scaled to separate various Hall contributions for $TmMn_6Sn_6$ as shown in Fig. 3(a) [11]. By fitting the linear parts where the ρ_{xy}^T term disappears, $R_0(T)$ and $S_H(T)$ are acquired as shown in Fig. 3(b). The ρ_{xy}^N and ρ_{xy}^A terms are calculated and subtracted from the total Hall resistivity to obtain ρ_{xy}^T.

The temperature dependences of ρ_{xy}^T are presented in Fig. 3(d). The prominent THE signal is observed in the high-temperature region and shrinks with decreasing T. Below 100 K, ρ_{xy}^T becomes invisible. Usually THE is considered to originate from the movement of skyrmions in noncentrosymmetric noncollinear magnets hosting nonzero scalar spin chirality. Recently, fluctuation-driven mechanisms were proposed to describe THE in centrosymmetric systems relating to a special nontrivial magnetic phase [9,11]. To further understand the THE in $TmMn_6Sn_6$, we first analyze its magnetic phase diagram. In our measurements, three regions are identified as shown in Fig. 3(c). According to previous results, with $\mu_0 H < \mu_0 H_{c1}$ the revealed distorted spiral (DS) orders dominate the magnetic structure in region 1 (above 50 K) [9]. With $\mu_0 H > \mu_0 H_s$, the saturated magnetization in the $M(\mu_0 H)$ curves suggests a forced ferromagnetic (FFM) state in region 3. In region 2, multiple possible magnetic transitions are suggested in region 2 by the observed disconnections in the differential field-dependent magnetization $dM/d(\mu_0 H)$ and peaks in ρ_{xy}^T for $TmMn_6Sn_6$. In its analog YMn_6Sn_6, transverse conical spiral (TCS) and fanlike (FL) states are observed in this region and the TCS state is considered to directly relate to THE [9]. In $TmMn_6Sn_6$, the suggested magnetic states are more complicated than those in YMn_6Sn_6. In addition, the observed THE for $TmMn_6Sn_6$ probably spans over several magnetic states exhibiting a strong $\mu_0 H$ response in contrast to that only observed in the TCS state for YMn_6Sn_6. Thus, besides large thermal fluctuations (such as those observed in YMn_6Sn_6) [25], possible nontrivial topological magnetic states cannot be excluded, which can also drive nonzero chirality leading to large THE. Further studies of the magnetic phase diagram by neutron scattering are necessary and expected to reveal the microscopic nature of THE in $TmMn_6Sn_6$.

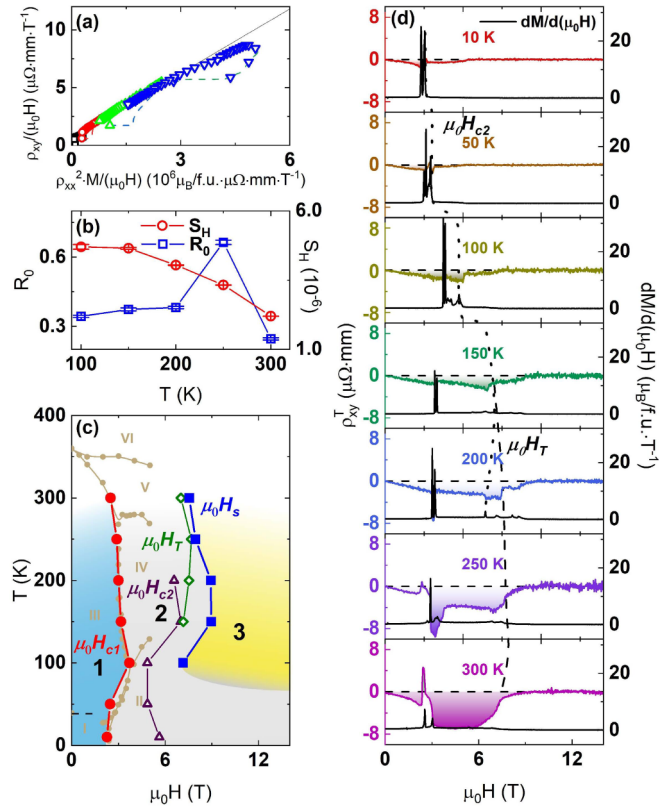

FIG. 3. (a) The scaling of $\rho_{xy}(\mu_0 H)/\mu_0 H$ curves as a function of $\rho_{xx}(\mu_0 H)^2 M(\mu_0 H)/\mu_0 H$ at 100, 150, 200, and 250 K. The black dashed line is the fitting curve by a linear function. (b) The temperature-dependent Hall coefficient $R_0(T)$ and intrinsic anomalous Hall coefficient $S_H(T)$. (c) The magnetic phase diagram of $TmMn_6Sn_6$. We roughly divide the whole phase diagram into three regions: region 1 marked by a blue shadow, region 2 marked by a light gray shadow, and region 3 marked by a yellow shadow. The data marked by light brown dots and lines are acquired from previous results which divide the phase diagram into several regions such as magnetic states I–VI [16]. The red circle line indicates the first flopping critical fields $\mu_0 H_{c1}$ recognized as the border between regions 1 and 2, and the blue line indicates saturated critical fields where $\mu_0 H_s$ is recognized as the border between regions 2 and 3. In region 2, more critical fields for abnormal features such as magnetic transitions are identified. $\mu_0 H_T$ (olive line) is a characteristic peak associated with THE. $\mu_0 H_{c2}$ (magenta line) is acquired from the most obvious peak of the differential curve of $dM/d(\mu_0 H)$ in region 2. (d) Field-dependent differential $dM/d(\mu_0 H)$ and $\rho_{xy}^T(\mu_0 H)$ at 10, 50, 100, 150, 200, 250, and 300 K.

B. Planar Hall effect and anisotropic magnetoresistivity

To investigate the planar properties of $TmMn_6Sn_6$, the applied field $\mu_0 H$ is rotated within the ac plane of the crystal as shown in Fig. 4(a). θ is defined as the angle between the current (I) along the c axis of the crystal and the applied magnetic field (when $\mu_0 H \parallel I \parallel c$, $\theta = 0°$, while when $\mu_0 H \perp a$, $\theta = 90°$). PHE, usually accompanied by PAMR, is a unique

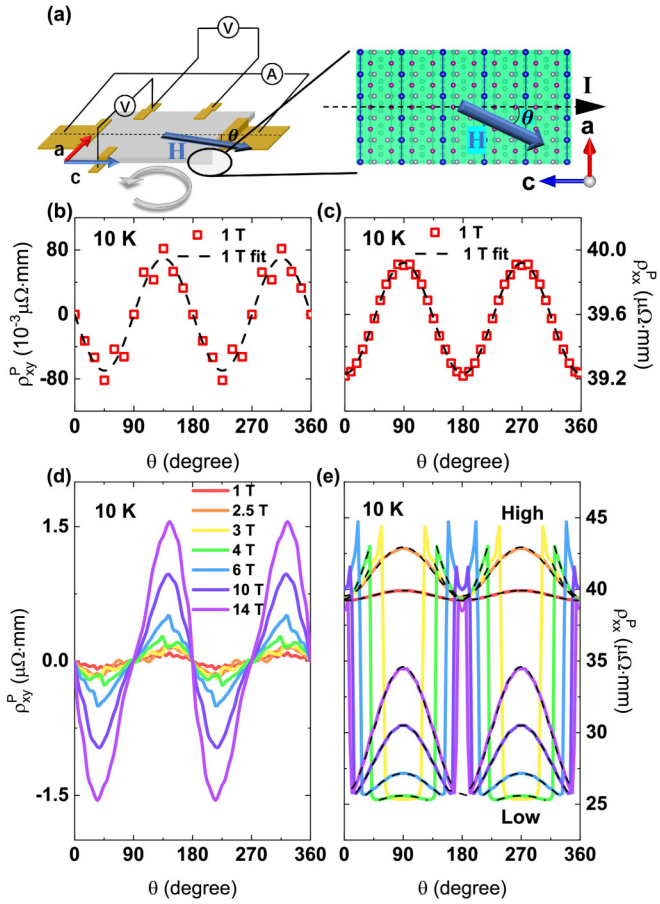

FIG. 4. (a) The configuration for planar transport measurements of a single crystal of $TmMn_6Sn_6$. The gray circular arrow indicates the rotating direction of the applied field. The current is along the c axis, and θ represents the angle between the applied field and current. (b) and (c) Angular-dependent planar Hall resistivity $\rho_{xy}^P(\theta)$ and planar longitudinal resistivity $\rho_{xx}^P(\theta)$ at 10 K with $\mu_0 H = 1$ T, respectively. The black dashed lines are the fitting curves by formula (2). (d) and (e) $\rho_{xy}^P(\theta)$ and $\rho_{xx}^P(\theta)$ at 10 K with $\mu_0 H = 1$, 2.5, 3, 4, 6, 10, and 14 T, respectively. $\rho_{xx}^P(\theta)$ is separated into "high" and "low" parts fitted by formula (4), marked by black dashed lines.

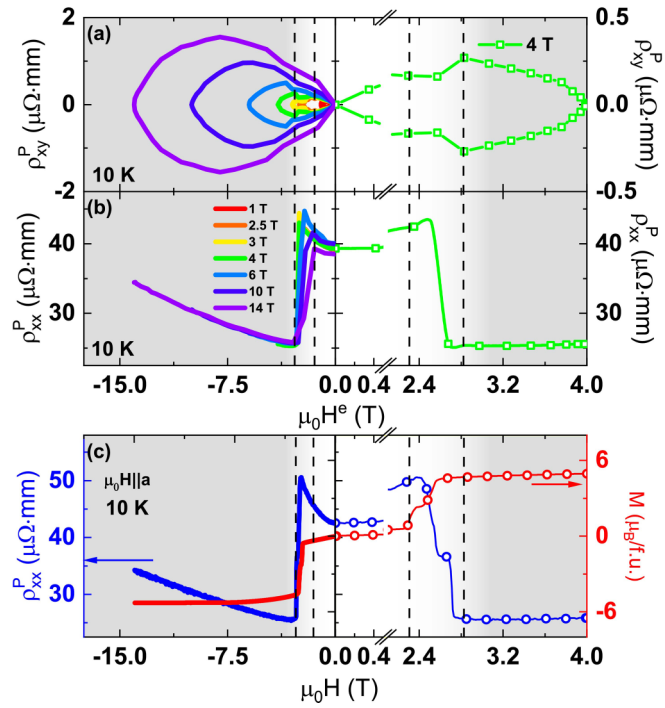

FIG. 5. (a) and (b) ρ_{xy}^P and ρ_{xx}^P vs $\mu_0 H^e$ ($\mu_0 H^e = \mu_0 H \sin\theta$) with $\mu_0 H = 1$, 2.5, 3, 4, 6, 10, and 14 T, respectively (left). ρ_{xy}^P and ρ_{xx}^P vs $\mu_0 H^e$ with $\mu_0 H = 4$ T around the region of $\mu_0 H^c \approx 2.4$ T (right). (c) The field-dependent magnetization $M(\mu_0 H)$ and the longitudinal resistivity $\rho_{xx}^P(\mu_0 H)$ vs $\mu_0 H^e$ at 10 K with $\mu_0 H \parallel c$. The zoomed $\rho_{xx}^P(\mu_0 H)$ and $M(\mu_0 H)$ at 10 K around a critical field of $\mu_0 H^c \approx 2.4$ T.

transport phenomenon driven by an in-plane magnetic-field-induced rotation of the principal axes of the resistivity tensor [26,27], which can detect the interplay of chirality, orbit, and spin for quantum materials. Usually, the PHE and PAMR can be described by empirical expressions as

$$\rho_{xy}^P = -\Delta\rho \sin\theta \cos\theta, \tag{2}$$

$$\rho_{xx}^P = \rho_{\parallel}^P + \Delta\rho \sin^2\theta, \tag{3}$$

where ρ_{xy}^P represents the in-plane Hall resistivity that directly shows the PHE, ρ_{xx}^P is the PAMR, and $\Delta\rho = \rho_{\perp}^P - \rho_{\parallel}^P$ is the resistivity anisotropy (called chiral resistivity in topological materials) with $\rho_{\perp}^P$ and $\rho_{\parallel}^P$ representing the resistivity with the $\mu_0 H$ perpendicular (90°) and parallel (0°) to the current, respectively [26]. At 10 K with $\mu_0 H = 1$ T, PHE and PAMR follow these empirical laws as shown in Figs. 4(b) and 4(c). The angular-dependent $\rho_{xy}^P(\theta)$ and $\rho_{xx}^P(\theta)$ exhibit twofold oscillations with a 45°-angle shift during an entire rotating period (from 0° to 360°). With increasing $\mu_0 H$, the amplitudes of oscillatory $\rho_{xy}^P(\theta)$ increase monotonously as shown in Fig. 4(d) and the angular dependence of ρ_{xy}^P deviates from the empirical relation. Correspondingly, sudden jumps are observed in $\rho_{xx}^P(\theta)$ curves separating the data into two groups ("high" and "low" parts). These jumps exhibit strong field and angular dependence. The behaviors for PHE and PAMR were barely observed and studied before which are considered to relate to magnetic transitions for $TmMn_6Sn_6$. To further investigate these PHE and PAMR, we define an effective field $\mu_0 H^e = \mu_0 H \sin\theta$ along the a axis which drives the carriers to move along its perpendicular direction by a Lorentz force within a semiclassical model. The $\rho_{xy}^P(\theta)$ and $\rho_{xx}^P(\theta)$ vs $\mu_0 H \sin\theta$ curves are presented in Fig. 5. Weak kinks are observed in the butterfly-shaped $\rho_{xy}^P(\theta)$ curves at an effective critical field of $\mu_0 H^c \approx 2.4$ T. Clearer features are observed in the $\rho_{xx}^P(\theta)$ curves in Fig. 5(b). The sharp drops at various angles from Fig. 4(e) are scaled together at the same critical effective field separating ρ_{xx}^P curves into two regions: (1) the high-resistivity part with $|\mu_0 H^e| < \mu_0 H^c$ and (2) the low-resistivity part with $|\mu_0 H^e| \geqslant \mu_0 H^c$. These behaviors are consistent with results acquired from the field-dependent resistivity $\rho_{xx}^P(\mu_0 H)$ and magnetization $M(\mu_0 H)$ with $\mu_0 H \parallel a$ exhibiting jumps or kinks around the magnetic flop transition from magnetic state 1 to state 2 [28]. The observed sudden jumps in $\rho_{xx}^P(\mu_0 H)$ indicate rotating the applied field can also drive the same magnetic flop transition from

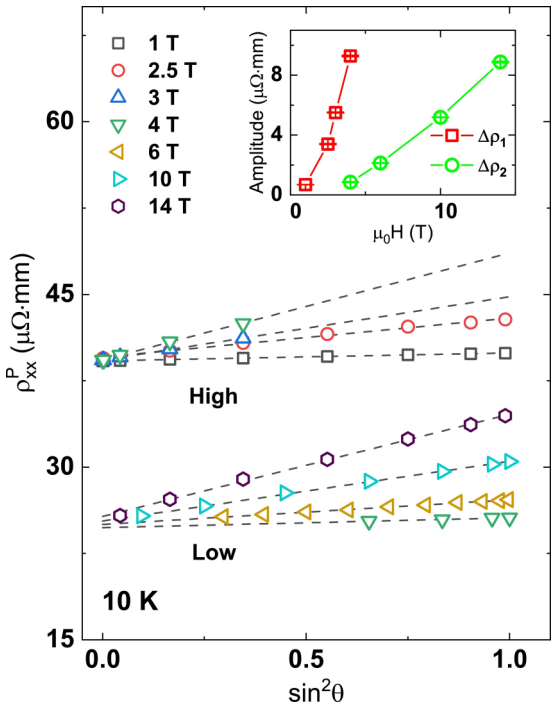

FIG. 6. ρ_{xx}^P as a function of $\sin^2\theta$ with $\mu_0 H = 1$, 2.5, 3, 4, 6, 10, and 14 T. $\rho_{xx}^P(\theta)$ is separated into high- and low-resistivity groups that use the relations $\rho_{xx} \sim \sin^2\theta$, where $\rho_{xx}^P(\theta)$ for each group is scaled together, indicating the PAMR in each magnetic state independently. Inset: $\Delta\rho_1$ (red line) and $\Delta\rho_2$ (green line) as functions of $\mu_0 H$ at 10 K.

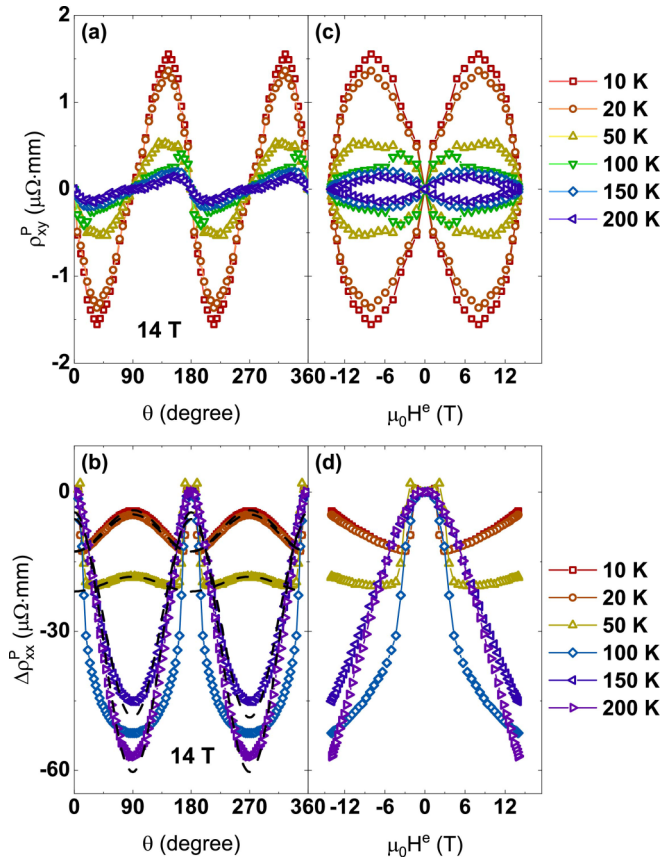

FIG. 7. (a) The PHE $\rho_{xx}^P(\theta)$ at 10, 20, 50, 100, 150, and 200 K with $\mu_0 H = 14$ T. (b) Angular dependence of $\Delta\rho_{xx}^P(\theta) = \rho_{xx}^P(\theta) - \rho_{xx}^P(0^\circ)$ at 10, 20, 50, 75, 100, 150, and 200 K with $\mu_0 H = 14$ T. The black dashed lines are the fitting curve. (c) The PHE $\rho_{xx}^P(\mu_0 H^e)$ as a function of $\mu_0 H^e = \mu_0 H \sin\theta$ at 10, 20, 50, 100, 150, and 200 K with $\mu_0 H = 14$ T. (d) $\Delta\rho_{xx}^P(\theta)$ as a function of $\mu_0 H^e$ at 10, 20, 50, 75, 100, 150, and 200 K with $\mu_0 H = 14$ T.

magnetic state 1 to state 2, which hosts different scatterings of carriers and changes the Zeeman gap leading to the different transport resistivities. To describe the PAMR in the presence of transitions, we can separate $\rho_{xx}^P(\theta)$ into the high- and low-resistivity groups which belong to magnetic states 1 and 2, respectively. Usually in a magnetic system, PAMR originates from the interaction of localized moments and spins of conduction electrons. In a single magnetic state, the interaction of the magnetic moment and spin-orbit coupling varies little for changing $\mu_0 H$, leading to $\rho_{xx}^P(\theta)$ following the same field and angle dependence. When the system transits to a new magnetic state, the changed interaction of the magnetic moments and the spin-orbit coupling will host a separated field and angle dependence for PAMR. In each magnetic state, PHE should exhibit oscillatory behavior similar to the empirical law. To check this idea, we plot $\rho_{xx}^P(\theta)$ vs $\sin^2\theta$ with various applied fields shown in Fig. 6. It is observed that the curves are separated into two groups, high and low, exhibiting a linear dependence of $\sin^2\theta$ for each group, indicating the PAMR in each magnetic state following the empirical formula independently. The amplitudes of oscillatory $\rho_{xx}^P(\theta)$ for the high- and low-resistivity groups are not the same usually and exhibit an independent increase with $\mu_0 H$ as shown in the inset of Fig. 6. To describe PAMR with a magnetic transition from magnetic state 1 to 2, an extended empirical expression is developed as

$$\rho_{xx}^P = [\rho_1^P + \Delta\rho_1 \sin^2\theta](|\mu_0 H^e| \leqslant \mu_0 H^c) + [\rho_2^P + \Delta\rho_2 \sin^2\theta](|\mu_0 H^e| \geqslant \mu_0 H^c), \quad (4)$$

where $\mu_0 H^e$ is the effective field, ρ_1^P and ρ_2^P are the values of high and low resistivity at $\theta = 0^\circ$, and $\Delta\rho_1$ and $\Delta\rho_2$ are the oscillatory amplitudes for different magnetic states. The data can be fitted by this formula shown in Fig. 4(e). Figure 7 shows the temperature dependence of $\rho_{xy}^P(\theta)$ and $\Delta\rho_{xx}^P(\theta)$ [defined as $\rho_{xx}^P(\theta) - \rho_{xx}^P(0^\circ)$] with $\mu_0 H = 14$ T. The derivations of the empirical laws are observed in both $\rho_{xy}^P(\theta)$ and $\Delta\rho_{xx}^P(\theta)$ curves, indicating the appearance of complicated magnetic states by changing T in Figs. 7(a) and 7(b). By using the same scaling technique, we analyze the planar transport properties evolving with changing T as shown in Figs. 7(c) and 7(d). The $\mu_0 H^c$ relating to the magnetic flop shifts to a lower-field region and becomes gradually invisible with increasing T. By using the extended formula, most of the curves are fitted with small derivations. In fact, with changing T the system undergoes multiple magnetic transitions even with the same $\mu_0 H$ resulting in various MR responses. With $\mu_0 H^e > \mu_0 H^c$ it is observed that the MR exhibits a positive response and evolves to a negative response gradually with changing T. Thus at some temperatures, rotating $\mu_0 H$ will drive more than two magnetic states with much broad transitions, which leads to a failure to fit $\rho_{xx}^P(\theta)$ by a general rule. For $TmMn_6Sn_6$, Tm

and Mn together construct the system's magnetic structure. The Tm^{3+} ions with $4f$ electron states provide a large magnetic moment ($7.6\mu_B$) [14], crystal field effect, and a strong magnetic interaction which hosts the richer magnetic states leading to our observed transport properties. Further investigations of detailed magnetic structures at various temperatures and fields are necessary and expected to reveal these exotic states.

IV. SUMMARY

We systematically studied the transport properties of the kagome magnet $TmMn_6Sn_6$. The observed prominent topological Hall effect in a wide temperature region suggests a nonzero spin chirality due to a complicated noncollinear magnetic structure with strong fluctuations. In the presence of magnetic transitions, the planar transport behavior (especially for PAMR) spanning over various magnetic states can be scaled within each magnetic state. Our results indicate the presence of multiple exotic magnetic states and provide an understanding of the planar transport behaviors for general magnetic materials with crossovers between different magnetic states.

ACKNOWLEDGMENTS

We thank Zhongbo Yan at Sun Yat-sen University for useful discussion. This work is supported by National Natural Science Foundation of China (NSFC) (Grants No. U213010013, No. 92165204, No. 11904414, and No. 12174454), Guangdong Basic and Applied Basic Research Foundation (Grants No. 2022A1515010035 and No. 2021B1515120015), open research fund of Songshan Lake materials Laboratory 2021SLABFN11, OEMT-2021-PZ-02, National Key Research and Development Program of China (No. 2019YFA0705702), and Physical Research Platform (PRP) in the School of Physics, Sun Yat-sen University.

[1] J. X. Yin, S. S. Zhang, H. Li, K. Jiang, G. Chang, B. Zhang, B. Lian, C. Xiang, I. Belopolski, H. Zheng, T. A. Cochran, S. Y. Xu, G. Bian, K. Liu, T. R. Chang, H. Lin, Z. Y. Lu, Z. Wang, S. Jia, W. Wang, and M. Z. Hasan, Nature (London) **562**, 91 (2018).

[2] L. Ye, M. Kang, J. Liu, F. Von Cube, C. R. Wicker, T. Suzuki, C. Jozwiak, A. Bostwick, E. Rotenberg, D. C. Bell, L. Fu, R. Comin, and J. G. Checkelsky, Nature (London) **555**, 638 (2018).

[3] E. Liu, Y. Sun, N. Kumar, L. Muechler, A. Sun, L. Jiao, S. Y. Yang, D. Liu, A. Liang, Q. Xu, J. Kroder, V. Süß, H. Borrmann, C. Shekhar, Z. Wang, C., W. Wang, W. Schnelle, S. Wirth, Y. Chen, S. T. B. Goennenwein, and C. Felser, Nat. Phys. **14**, 1125 (2018).

[4] M. Kang, L. Ye, S. Fang, J. S. You, A. Levitan, M. Han, J. I. Facio, C. Jozwiak, A. Bostwick, E. Rotenberg, M. K. Chan, R. D. McDonald, D. Graf, K. Kaznatcheev, E. Vescovo, D. C. Bell, E. Kaxiras, J. van den Brink, M. Richter, M. Prasad Ghimire, J. G. Checkelsky, and R. Comin, Nat. Mater. **19**, 163 (2020).

[5] Y. Kasahara, T. Ohnishi, Y. Mizukami, O. Tanaka, Sixiao Ma, K. Sugii, N. Kurita, H. Tanaka, J. Nasu, Y. Motome, T. Shibauchi, and Y. Matsuda, Nature (London) **559**, 227 (2018).

[6] E. Tang, J. W. Mei, and X. G. Wen, Phys. Rev. Lett. **106**, 236802 (2011).

[7] K. Ohgushi, S. Murakami, and N. Nagaosa, Phys. Rev. B **62**, R6065 (2000).

[8] X. Xu, J. X. Yin, W. Ma, H. J. Tien, X. B. Qiang, P. V. Sreenivasa Reddy, H. Zhou, J. Shen, H. Z. Lu, T. R. Chang, Z. Qu, and S. Jia, Nat. Commun. **13**, 1197 (2022).

[9] N. J. Ghimire, R. L. Dally, L. Poudel, D. C. Jones, D. Michel, N. T. Magar, M. Bleuel, M. A. Mcguire, J. S. Jiang, J. F. Mitchell, J. W. Lynn, and I. I. Mazin, Sci. Adv. **6**, eabe2680 (2020).

[10] M. Li, Q. Wang, G. Wang, Z. Yuan, W. Song, R. Lou, Z. Liu, Y. Huang, Z. Liu, H. Lei, Z. Yin, and S. Wang, Nat. Commun. **12**, 3129 (2021).

[11] Q. Wang, K. J. Neubauer, C. Duan, Q. Yin, S. Fujitsu, H. Hosono, F. Ye, R. Zhang, S. Chi, K. Krycka, H. Lei, and P. Dai, Phys. Rev. B **103**, 014416 (2021).

[12] W. Ma, X. Xu, J. X. Yin, H. Yang, H. Zhou, Z. J. Cheng, Y. Huang, Z. Qu, F. Wang, M. Z. Hasan, and S. Jia, Phys. Rev. Lett. **126**, 246602 (2021).

[13] L. Gao, S. Shen, Q. Wang, W. Shi, Y. Zhao, C. Li, W. Cao, C. Pei, J. Y. Ge, G. Li, J. Li, Y. Chen, S. Yan, and Y. Qi, Appl. Phys. Lett. **119**, 092405 (2021).

[14] G. Venturini, B. C. El Idrissi, and B. Malaman, J. Magn. Magn. Mater. **94**, 35 (1991).

[15] B. Malaman, G. Venturini, R. Welter, J. P. Sanchez, P. Vulliet, and E. Ressouche, J. Magn. Magn. Mater. **202**, 519 (1999).

[16] D. M. Clatterbuck and K. A. Gschneidner, Jr., J. Magn. Magn. Mater. **207**, 78 (1999).

[17] B. Malaman, G. Venturini, and B. Roques, Mater. Res. Bull. **23**, 1629 (1988).

[18] Y. Sawai, K. Kindo, L. Zhang, J. C. P. Klaasse, E. Brück, K. H. J. Buschow, F. R. de Boer, C. Lefèvre, and G. Venturini, J. Alloys Compd. **408-412**, 196 (2006).

[19] L. K. Perry, D. H. Ryan, G. Venturini, and B. Malaman, J. Alloys Compd. **469**, 34 (2009).

[20] S.-W. Cheong and X. Xu, npj Quantum Mater. **7**, 40 (2022).

[21] C. Lefèvre, G. Venturini, and B. Malaman, J. Alloys Compd. **346**, 84 (2002).

[22] N. Nagaosa and Y. Tokura, Nat. Nanotechnol. **8**, 899 (2013).

[23] P. K. Rout, P. V. Prakash Madduri, S. K. Manna, and A. K. Nayak, Phys. Rev. B **99**, 094430 (2019).

[24] N. Nagaosa, J. Sinova, S. Onoda, A. H. MacDonald, and N. P. Ong, Rev. Mod. Phys. **82**, 1539 (2010).

[25] A. Neubauer, C. Pfleiderer, B. Binz, A. Rosch, R. Ritz, P. G. Niklowitz, and P. Böni, Phys. Rev. Lett. **110**, 209902(E) (2013).

[26] K. M. Koch, Z. Naturforsch. A **10**, 496 (1955).

[27] C. Goldberg and R. E. Davis, Phys. Rev. **94**, 1121 (1954).

[28] R. L. Dally, J. W. Lynn, N. J. Ghimire, D. Michel, P. Siegfried, and I. I. Mazin, Phys. Rev. B **103**, 094413 (2021).